RSC Advances

ROYAL SOCIETY OF CHEMISTRY

www.rsc.org/advances

Journal Name

RSC Advances

ARTICLE TYPE

g-C$_3$N$_4$/Bi$_4$O$_5$I$_2$ 2D-2D heterojunctional nanosheets with enhanced visible-light photocatalytic activity

Na Tian, Yihe Zhang*, Chengyin Liu, Shixin Yu, Min Li, Hongwei Huang*

5

We disclose the fabrication of 2D-2D heterojunctional nanosheets g-C$_3$N$_4$/Bi$_4$O$_5$I$_2$ photocatalyst by using a mixed-calcination method. This synthetic method enables intimate interfacial interaction between g-
10 C$_3$N$_4$ and Bi$_4$O$_5$I$_2$, which is beneficial for charge transfer at the interface. The photocatalysis properties of g-C$_3$N$_4$/Bi$_4$O$_5$I$_2$ composites were studied by photodegradation of Rhodamine B (RhB) and NO removal under visible-light (λ > 420 nm) irradiation. The results revealed that the g-C$_3$N$_4$/Bi$_4$O$_5$I$_2$ composite show enhanced photocatalytic activity compared to the pristine g-C$_3$N$_4$ and Bi$_4$O$_5$I$_2$ samples. Investigations on the behaviours of charge carriers via photoluminescence (PL) spectra and transient photocurrent
15 responses suggests that the g-C$_3$N$_4$/Bi$_4$O$_5$I$_2$ heterostructure is responsible for the efficient separation and transfer of photogenerated electron-hole pairs, thus giving rise to the higher photocatalytic activity. The formation of 2D-2D heterostructured *n-n* type g-C$_3$N$_4$/Bi$_4$O$_5$I$_2$ composites as well as photocatalytic mechanism was verified by a series of combined techniques, including the active species trapping experiments and Mott-Schottky plots. The present work furthered our understanding on fabrication of
20 homogeneous heterojunction photocatalyst.

1. Introduction

Nowadays, environmental pollution and the energy crisis are two major problems in human society which seriously threaten the existence of terrestrial lives.[1,2] In the past two decades,
25 numerous investigations have focused on semiconductor-based photocatalysts because they may be widely applied for solar energy conversion and environmental purification. To date, many semiconductors have been extensively studied as photocatalysts for degrading pollutants or splitting water.[3,4] However, wide
30 band gap semiconductors, such as TiO$_2$, ZnO, and SnO$_2$ are only able to absorb < 5% of the solar radiation that reaches the earth's surface, while narrow band gap semiconductors, such as Fe$_2$O$_3$, CuO, and CdS usually exhibit poor photocatalytic performance due to their high carrier recombination rate, low electronic
35 conduction, low oxidation, or poor photostability, which greatly limits their practical applications.[5-7] Therefore, the development of novel, highly efficient, persistently stable, and visible light driven photocatalysts remains a major challenge.

Recently, the bismuth oxyhalides (BiOX, X=Cl, Br, and I),[8-
40 10] have demonstrated remarkable photocatalytic activities because their uniquely layered structure features an internal static electric field perpendicular to each layer that may induce more effective separation of photogenerated charge carriers. Among which, BiOI has the smallest band gap and a strong absorption in
45 the visible light region, thus demonstrating excellent photocatalytic efficiency under sunlight irradiation. Apart from

BiOI (O:I = 1:1), other I-poor bismuth oxyiodides, including Bi$_4$O$_5$I$_2$, Bi$_7$O$_9$I$_3$, α-Bi$_5$O$_7$I, and β-Bi$_5$O$_7$I, have also been reported.[11-13] Since the valence band for bismuth oxyiodides
50 mostly contains O 2p and I 5p orbitals, while the conduction band is based the Bi 6p orbital, it can be predicted that the I-poor bismuth oxyiodides have band gap energies that are higher than BiOI but lower than Bi$_2$O$_3$. Therefore, these materials may be used as visible light induced photocatalysts. Bi$_4$O$_5$I$_2$ is a newly
55 found visible-light-driven photocatalyst, which was prepared by a hydrolytic method. We synthesized this oxygen-rich bismuth oxyiodieds (Bi$_4$O$_5$I$_2$) using commercial Bi(NO$_3$)$_3$·5H$_2$O, ethylene glycol, KI, and NaOH under hydrolytic conditions. And as a new family of promising photocatalysts, Bi$_4$O$_5$I$_2$ displayed relatively
60 high efficient photocatalytic activity in the decomposition of rhodamine B (RhB) in water and NO in air under visible light. However, there still exist some drawbacks in Bi$_4$O$_5$I$_2$, such as deficient light absorption, low transfer efficiency of photogenerated charge carriers in the local two-dimensional (2D)
65 crystal structure of Bi$_4$O$_5$I$_2$, etc. Therefore, construction of heterojunctional structure by combining Bi$_4$O$_5$I$_2$ with other appropriate semiconductors may be a constructive and instructive method to further improve the photocatalytic activity of Bi$_4$O$_5$I$_2$.

As a marvelous earth-abundant visible light photocatalyst,
70 graphitic carbon nitride (g-C$_3$N$_4$) possesses a particular two-dimensional (2D) structure, unique electronic structure and outstanding chemical stability.[14,15] Pure g-C$_3$N$_4$ suffers from rapid recombination of photoexcited electron-hole pairs, which

confoundedly resulted in low photocatalytic activity. Due to the superb electronic structure, the g-C_3N_4 could act as a prominent candidate for coupling with various potential semiconductors to enhance the photocatalytic performance, such as $BiVO_4$/g-C_3N_4,[16] $AgCO_3$/g-C_3N_4,[17] CeO_2/g-C_3N_4,[18] and BiOX(X=Cl, Br, I)/g-C_3N_4.[19-21] Up to now, the g-C_3N_4 based heterojunction enjoy a fierce development on the application of water purification, photocatalytic hydrogen evolution, carbon dioxide reduction, and supercapacitors. For the exploration of g-C_3N_4-based nanocomposites is far from over, and it is worth of a deep and thorough research.

In this paper, the hierarchical photocatalyst composites combining two-dimensional $Bi_4O_5I_2$ nanoflakes and g-C_3N_4 nanosheets were synthesized using a simple mixed-calcination route. Their structure, morphology, band structure, and optical properties were characterized. The photocatalytic performance of g-C_3N_4/$Bi_4O_5I_2$ composites were evaluated by studying RhB degradation and NO removal under visible light (λ > 420 nm) irradiation. In addition, the possible photocatalytic mechanism was proposed by trapping the photogenerated reactive species.

2. Experimental Section

2.1 Synthesis of g-C_3N_4/$Bi_4O_5I_2$ photocatalyst.

All chemical reagents were used as purchased without further purification. Pure g-C_3N_4 sample was synthesized by calcining melamine in a muffle furnace at 520 °C for 4 h. Pure $Bi_4O_5I_2$ was prepared via a simple hydrothermal method as following: 1.5 mmol $Bi(NO_3)_3 \cdot 5H_2O$ was dissolved in 35 mL ethylene glycol to form solution A, and 3 mmol KI was dissolved in 20 mL distilled water to form solution B. After the solution B was dropwisely added into solution A with vigorously string, NaOH solution (2 mol/L) was used to adjust the pH value to 7, and continuously string for 30 min. Then the above mixture were transferred into a 100 mL Teflon-lined stainless steel autoclave and maintained at 150 °C for 12 h. Followed by cooling to room temperature and the resulting powders were collected and washed with alcohol and distilled water for three times, and dried at 60 °C for 10 h. The g-C_3N_4/$Bi_4O_5I_2$ composites were fabricated through a mix-calcining route. The g-C_3N_4 and $Bi_4O_5I_2$ with given ratios (molar ratios of g-C_3N_4/$Bi_4O_5I_2$ = 4:6, 3:7, 5:5) were mixed and ground for 10 min, and then calcined at 450 °C for 4 h. In order to keep a consistent experimental condition, the pristine g-C_3N_4 and $Bi_4O_5I_2$ were also calcined at 450 °C for 4 h.

2.2 Characterization

The crystalline structures of the samples were determined using powder X-ray diffraction (XRD) with a Bruker D8 Advance (Bruker AXS, Germany) X-ray diffracts to meter with Cu Kα. The Fourier transform infrared (FTIR) spectra of the sample were recorded on a Bruker spectrometer in the frequency range of 4000-450 cm^{-1}. X-ray photoelectron spectroscopy with Al Ka X-rays (ht = 1486.6 eV) irradiation operating at 150 W (XPS: Thermo ESCALAB 250, USA) was used to study the surface properties of the samples. The spectra were recorded at room temperature in air ranged from 370 nm to 700 nm. The scanning electron microscopy (SEM) on a Hitachi S-4800 instrument was employed to observe the morphologies of the photocatalysts.

Transmission electron microscopy (TEM) images and high-resolution transmission electron microscopy (HRTEM) images were taken on a JEM 2100F microscope, using an accelerating voltage of 200 kV. The UV-visible diffuse-reflectance spectra (UV-vis DRS) were measured by a Varian Cary 5000 UV-vis spectrophotometer. The Brunauer-Emmett-Teller (BET) surface area was measured with an ASAP2020 specific surface area and porosity analyzer. Photoluminescence spectra (PL) of the samples were obtained using a fluorescence spectrometer (Hitachi F-4600) at room temperature.

2.3 photocatalytic evaluation.

The organic Rhodamine B (RhB) was chosen as a representative model pollutant to evaluate the photocatalytic performance of the samples. In each experiment, 0.5g photocatalyst was added into 50mL RhB solution ($1*10^{-5}$ mol•L^{-1}) in quartz tubes. Prior to irradiation, the suspensions were stirred in the dark for 30min to reach adsorption-desorption equilibrium between the photocatalyst and RhB. The concentrations of RhB supernatants after centrifuged were analysed using a UV-vis spectrophotometer (Cary 5000) in a certain time interval, and the total organic carbon (TOC) contents of them were measured by a total organic carbon analyser (TOC, Shimadzu 500).

The photocatalytic activity was also investigated by removal of NO at ppb levels in a continuous flow reactor at ambient temperature. The volume of the rectangular reactor, made of stainless steel and covered with Saint-Glass, was 4.5 L (30 cm × 15 cm × 10 cm). A 300 W commercial tungsten halogen lamp was vertically placed outside the reactor. For the visible light photocatalytic activity test, UV cut-off filters (420 nm) ware adopted to remove UV light in the light beam. Photocatalyst (0.15 g) was coated onto a dish with a diameter of 12.0 cm. The coated dish was then pretreated at 70 °C to remove water in the suspension. The NO gas was acquired from a compressed gas cylinder at a concentration of 100 ppm of NO with traceable National Institute of Standards and Technology (NIST) standard. The initial concentration of NO was diluted to about 450 ppb by the air stream supplied by a zero air generator (Thermo Environmental Inc., model 111). The desired relative humidity (RH) level of the NO flow was controlled at 70% by passing the zero.

2.4 Active species trapping experiment

For the purpose of revealing the active species in the photocatalytic process, disodium ethylenediaminetetraacetate (EDTA), tert-butyl alcohol (TBA), and 1,4-benzoquinone (BQ) were chosen as hole (h$^+$) scavenger, hydroxyl radical (•OH) scavenger, and superoxide radical (•O$_2^-$) scavenger, respectively.[22-24] Moreover, in order to resolve whether molecular oxygen (O_2) was involved in the photodegradation reaction, O_2 was eliminated by bubbling high-purity nitrogen in this process. Typically, 50 mg photocatalyst with different scavengers (1 mmol) were dispersed in RhB aqueous solution (50 mL, $1*10^{-5}$ mol•L^{-1}), and the following processes are similar to the RhB photodegradation experiment.

2.5 Photoelectrochemical measurements experiments.

Photoelectrochemical measurements were performed on an

electrochemical analyzer (CHI660E, CHI Shanghai, Inc.) in a standard three-electrode configuration with a Pt wire as the counter electrode and Hg/Hg_2Cl_2 (in saturated KCl) as a reference electrode. Irradiation proceeded with a Xe arc lamp. Na_2SO_4 (0.1 mol•L^{-1}) aqueous solution was used as the electrolyte. The typical working electrode was prepared as follows: 10 mg ground sample was mixed with 1 mL alcohol to make slurry. The slurry was then dispersed onto a 2 cm × 1 cm ITO glass and then the ITO glass was dried at 60°C for 10 h to obtain the electrode.

3. Results and discussion

3.1. Characterization

3.1.1 Characterization of Composite Photocatalysts.

Fig. 1a shows the XRD patterns of the pristine g-C_3N_4, $Bi_4O_5I_2$, and g-C_3N_4/$Bi_4O_5I_2$ composites synthesized in this work. The XRD peaks of pure g-C_3N_4 and $Bi_4O_5I_2$ can be indexed to tetragonal phase g-C_3N_4 (JCPDS: 87-1526)[16] and monoclinic phase $Bi_4O_5I_2$,[11,25] respectively. Two distinct diffraction peaks at 27.40° and 13.04° can be assigned to the corresponding (002) and (100) diffraction planes of the g-C_3N_4.[11,24] No impurity peaks were observed, which implies that the final products of g-C_3N_4 and $Bi_4O_5I_2$ were of pure phases. The XRD patterns of all the g-C_3N_4/$Bi_4O_5I_2$ samples were similar to that of pure $Bi_4O_5I_2$, which is due to the low intensity of g-C_3N_4. Fig. 1b shows the FTIR spectra of g-C_3N_4, $Bi_4O_5I_2$ and g-C_3N_4/$Bi_4O_5I_2$ to investigate the chemical bonding of the as-prepared samples. The intense bands in the 900–1200 cm^{-1} region can be assigned to the typical stretching modes of CN heterocyclic. And the pointy peak at 807 cm^{-1} represents the out of plane breathing vibration characteristic of triazine unites.[26,27] Moreover, the peak at 3430 cm^{-1} was attributed to the existence of water. As for the pristine $Bi_4O_5I_2$, the series of peaks at 598–1108 cm^{-1} were attributed to the stretching vibrations of the Bi-O, while the peaks located at 1377 cm^{-1} were assigned to the stretching vibrations of I-O. In the case of the g-C_3N_4/$Bi_4O_5I_2$ composites, all of the spectra exhibit the characteristic peaks of both g-C_3N_4 and $Bi_4O_5I_2$, indicating the successful combination of the two components.

Morphology and microstructure of the as-synthesized g-C_3N_4/$Bi_4O_5I_2$ composites were characterized. It can be observed from Fig. 1S that the as-synthesized $Bi_4O_5I_2$ (Fig. 1Sa and c) displays a two-dimensional (2D) nanostructure with numerous nanoflakes. These 2D samples are connected to each other with less than 15 nm in thickness and 50-200 nm in other two dimensions (Fig. 1Sa). From the SEM images of g-C_3N_4 (Fig. 1Sb), we can observe that g-C_3N_4 nanosheets are randomly combined with each other, and showing a bulk morphology. The existence of $Bi_4O_5I_2$ nanosheets on g-C_3N_4 would expedite the formation of heterojunction interface between g-C_3N_4 and $Bi_4O_5I_2$. The microstructure was further studied by TEM (Fig. 2). Fig. 2a and c confirmed the structures of g-C_3N_4 nanosheets and $Bi_4O_5I_2$ nanoflakes. The TEM image of 3-7 g-C_3N_4/$Bi_4O_5I_2$ sample in Fig. 2c not only shows the sheet-like g-C_3N_4, but also depicts the front and side view of $Bi_4O_5I_2$ nanoflakes. The corresponding high-resolution TEM image shown in Fig. 2d depicts a clearly resolved crystalline domain with a uniform

interplanar spacing of 0.305 nm, corresponding to the (-4-11) plane of the monoclinic $Bi_4O_5I_2$.

The XPS analysis was used to investigate the surface chemical state of elements in the pure $Bi_4O_5I_2$ and g-C_3N_4, and 3-7 g-C_3N_4/$Bi_4O_5I_2$ composites, respectively. Bi, I, O, C and N are all successfully detected in 3-7 g-C_3N_4/$Bi_4O_5I_2$ (Fig. 3a), indicating that the as-prepared composite is formed. Fig. 3b~d show the high-resolution XPS spectra of Bi 4f, I 3d and O 1s for pure $Bi_4O_5I_2$ and 3-7 g-C_3N_4/$Bi_4O_5I_2$, respectively. As can be seen from Fig. 3d, the binding energies of Bi $4f_{5/2}$ and Bi $4f_{7/2}$ for pure $Bi_4O_5I_2$ are 164.85 and 159.53 eV, respectively. While those for 3-7 g-C_3N_4/$Bi_4O_5I_2$ are 164.28 and 158.96 eV, respectively, showing that the value of the two peaks reduced. The peaks centered at 631.18 eV and 619.73 eV are ascribed to I $3d_{5/2}$, and I $3d_{3/2}$, for the pure $Bi_4O_5I_2$. Similar to the element of Bi, the position of the peaks shift to 630.51 eV and 618.98 eV for the 3-7 g-C_3N_4/$Bi_4O_5I_2$ composites. In Fig. 3d, for the pure $Bi_4O_5I_2$ and 3-7 g-C_3N_4/$Bi_4O_5I_2$, O 1s and O-H signals can be detected, respectively, evidencing the oxygen atoms and the hydroxyl (O-H) groups attached on the surface of samples [28]. The shift of Bi 4f, I 3d and O 1s peaks implied that the formation of g-C_3N_4/$Bi_4O_5I_2$ heterojunctions. Fig. 3e and f show the high-resolution XPS spectra of C 1s and N 1s for pure g-C_3N_4 and 3-7 g-C_3N_4/$Bi_4O_5I_2$, respectively. In Fig. 3e, the peak of C 1s at 284.78 eV is the characteristic of the adventitious carbon on the surface of g-C_3N_4 and 3-7 g-C_3N_4/$Bi_4O_5I_2$, and the peaks at 288.39 eV are attributed to the sp^2 hybridized C (C-$(N)_3$).[29] It can be clearly seen that the 3-7 g-C_3N_4/$Bi_4O_5I_2$ appears a new peak at 285.64 eV, which was also assigned to the sp^2 hybridized C (C-$(N)_3$).[29] And for the 3-7 g-C_3N_4/$Bi_4O_5I_2$, the intensity of the peak at 284.78 eV is weaker than the pure g-C_3N_4, while that at 288.39 eV is stronger. These all above may indicate the strong interaction between g-C_3N_4 and $Bi_4O_5I_2$. The main features of N 1s are shown in Fig. 3f and a peak at 398.69 eV can be seen, which attributed to the existence of sp^2-bonded g-C_3N_4 in the 3-7 g-C_3N_4/$Bi_4O_5I_2$ composites, reflecting the sp^2-hybridized nitrogen (C=N-C).[28] The two peaks observed at 399.50 eV and 401.07 eV were assigned to tertiary nitrogen (N-(C_3)) groups and the effects of charging reaction, respectively.[30] The XPS results confirmed the formation of the g-C_3N_4/$Bi_4O_5I_2$ heterostructure.

The BET surface area of g-C_3N_4, $Bi_4O_5I_2$ and g-C_3N_4/$Bi_4O_5I_2$ composites are given in Table S1. The surface area of g-C_3N_4 (4.25 m^2/g), which is much lower than that of $Bi_4O_5I_2$ (23.45 m^2/g). With increasing the content of g-C_3N_4, the surface area of g-C_3N_4/$Bi_4O_5I_2$ gradually decreases, and these values are 17.23, 13.77 and 10.21 for 3-7 g-C_3N_4/$Bi_4O_5I_2$, 4-6 g-C_3N_4/$Bi_4O_5I_2$ and 5-5 g-C_3N_4/$Bi_4O_5I_2$.

Optical absorption of a semiconductor photocatalyst is an important factor in determining the photocatalytic performance. Fig. 4 shows the UV-vis DRS of pristine g-C_3N_4, $Bi_4O_5I_2$, and as-prepared g-C_3N_4/$Bi_4O_5I_2$ samples. Pure g-C_3N_4 presents relatively weaker visible light absorption ability with absorption edge of about 459 nm, whereas $Bi_4O_5I_2$ shows good visible light absorption with absorption edge longer than 520 nm. In contrast to g-C_3N_4, the absorption edge of the composites shifts monotonically to longer wavelengths as the amount of $Bi_4O_5I_2$ increases. This result suggests that the photoabsorption of g-C_3N_4

can be enhanced by $Bi_4O_5I_2$. For the semiconductor, the absorption of light is determined by band gap, which can be obtained by the following formula:

$$\alpha h\nu = A(h\nu - E_g)^{n/2} \qquad (1)$$

where α, h, ν and E_g are the optical absorption coefficient, Plank constant, photonic frequency, band gap, respectively, and A is a proportionality constant.[31,32] In this equation, when the transition type of semiconductor is direct transitions, the n value is 1. Otherwise, n value is 4 for indirect transitions. The samples of g-C_3N_4 and $Bi_4O_5I_2$ are both ascribed to indirect transitions, so the n value is given as 4. Based on the plots of $(\alpha h\nu)^{1/2}$ versus hν, band gaps (E_g) of g-C_3N_4 and $Bi_4O_5I_2$ are separately estimated to 2.70 and 2.03 eV. After combination between g-C_3N_4 and $Bi_4O_5I_2$, the heterojunction of (2-8, 3-7, 4-6) g-C_3N_4/$Bi_4O_5I_2$ are all attributed to indirect transitions (n=4). Thence the E_g of 2-8 g-C_3N_4/$Bi_4O_5I_2$, 3-7 g-C_3N_4/$Bi_4O_5I_2$, and 4-6 g-C_3N_4/$Bi_4O_5I_2$ are estimated to 2.70, 2.76, and 2.03 eV, respectively, as show in the inset of Fig. 4.

3.2. Photocatalytic activities.

The photodegradation of organic Rhodamine B (RhB, anionic dye) under visible-light illumination ($\lambda > 420$ nm) was used to evaluate the photocatalytic property of the obtained photocatalysts, which is shown in Fig. 5a. It can be seen that all composites show higher activity than g-C_3N_4, and the 3-7 g-C_3N_4/$Bi_4O_5I_2$ shows the best photocatalytic performance among the samples, which can degrade RhB completely in 30 min. The pseudo-first-order kinetic curves of RhB photodegradation were also plotted to analyze the degradation rate quantitatively. The experimental data clearly displayed that the apparent rate constant k is 0.057 min^{-1}, 0.060 min^{-1}, 0.112 min^{-1}, 0.045 min^{-1}, and 0.021 min^{-1}, for the pristine g-C_3N_4, $Bi_4O_5I_2$ and g-C_3N_4/$Bi_4O_5I_2$ composites with molar ratios of 2:8, 3:7, 4:6, respectively (insert of Fig. 5a). In other words, the photocatalytic activity of 3:7 g-C_3N_4/$Bi_4O_5I_2$ is 1.96 and 5.33 times higher than those of single g-C_3N_4 and $Bi_4O_5I_2$, respectively. During 40 min of visible light irradiation, 99% of RhB ($1*10^{-5}$ mol•L^{-1}) is photodegraded using 1 g/L of 3-7 g-C_3N_4/$Bi_4O_5I_2$.

For practical applications, the effective mineralization of contaminants throughout the photocatalytic process is critical to avoid secondary pollution. Total organic carbon (TOC) was selected as the mineralization index for this system, and the time independence of the TOC in the RhB solution during the photoreaction is displayed in Fig. 5b. As shown in Fig. 5b, the determined TOC values are calculated into TOC removal curves. It can be observed that the TOC removal of RhB solution over the as-synthesized g-C_3N_4/$Bi_4O_5I_2$ heterojunctions have remarkable ascent within 40 min under the visible-light irradiation, suggesting their efficient mineralization properties.[33] The TOC removal rate of 3-7 g-C_3N_4/$Bi_4O_5I_2$ reaches the highest, 92%. With the g-C_3N_4 content increasing, the mineralization efficiencies exhibit a rise first and then a decline, illustrating that there is an appropriate composite ratio between g-C_3N_4 and $Bi_4O_5I_2$. These results entirely correspond with those in Fig. 5a.

The photooxidation capacity of the pure $Bi_4O_5I_2$, g-C_3N_4 and g-C_3N_4/$Bi_4O_5I_2$ composites was further evaluated by NO removal under visible light irradiation (shown in Fig. 5c). The adsorption-desorption equilibrium was reached in the dark before the lamp was turned on. In other words, the concentration of NO was kept constant, and then the light was switched on to illuminate the photocatalyst and initiate the photocatalytic reaction. As shown in Fig. 5c, the optimal photocatalytic activity was also achieved for 3-7 g-C_3N_4/$Bi_4O_5I_2$, which shows a NO removal rate of 51% after 30 min illumination. This may be attributed to the balance between optical absorption, surface area and charge separation efficiency of the g-C_3N_4/$Bi_4O_5I_2$ heterojunctions.

Fig. 5d shows results from the trapping experiment of active species during the photocatalytic reaction under irradiation. It can be seen that the photocatalytic degradation of RhB decreased obviously with the addition of 1,4-benzoquinone (BQ, a quencher of $•O_2^-$) and ethylenediaminetetraacetate (EDTA, a quencher of h$^+$), but was almost not affected by the addition of 1mM tert-butyl alcohol TBA (a quencher of •OH). It indicates that h$^+$ and $•O_2^-$ are the main active species rather than •OH under visible-light irradiation. In addition, we also studied the role of molecular oxygen on over 3-7 g-C_3N_4/$Bi_4O_5I_2$ by bubbling high-purity nitrogen to eliminate O_2 during the photocatalysis. It was found that the RhB photocatalytic degradation on 3-7 g-C_3N_4/$Bi_4O_5I_2$ was obviously depressed (Fig. 5d), suggesting that molecular oxygen was involved in RhB photocatalytic degradation with g-C_3N_4/$Bi_4O_5I_2$.

3.3. Mechanism investigation on the enhanced photocatalytic activity.

The schematic diagram of charge separation of g-C_3N_4/$Bi_4O_5I_2$ was proposed and illustrated in Fig. 6. The enhanced photocatalytic activity of g-C_3N_4/$Bi_4O_5I_2$ can be explained as follows: Under visible light ($\lambda > 420$ nm) irradiation, $Bi_4O_5I_2$ and g-C_3N_4 could be easily excited, and electrons and holes appeared in the CB and VB, respectively. Then the VB holes of $Bi_4O_5I_2$ are migrated to the VB of g-C_3N_4, while the electrons gathered at the CB of $Bi_4O_5I_2$ from the CB of g-C_3N_4. Hence, the electron-hole recombination process is suppressed and the life time of the charge carriers are extended at the *n-n* type heterojunction. The electrons, which were accumulated on the CB of $Bi_4O_5I_2$, react with surface adsorbed oxygen to form super oxide radicals ($•O_2^-$). The reactive species ($•O_2^-$ and h$^+$) formed in the photocatalytic process are responsible for the degradation of RhB and NO removal. Therefore, formation of *n-n* heterojunction with efficient electron-hole separation enhanced the photocatalytic activity of g-C_3N_4/$Bi_4O_5I_2$ composites.

To investigate the separation and transfer efficiency of charge carriers generated in the photocatalysts, the photocurrent response is obtained after three on-off cycles of visible light irradiation.[34-36] Fig. 7 shows the photocurrent densities of the pure g-C_3N_4 and $Bi_4O_5I_2$, and 3-7 g-C_3N_4/$Bi_4O_5I_2$ composites heterojunctions under visible light. When the light is turned on, immediate photocurrent response can be observed. The 3-7 g-C_3N_4/$Bi_4O_5I_2$ heterojunction shows a much larger photocurrent density than the pure g-C_3N_4 and $Bi_4O_5I_2$. The photocurrent amplitudes of the three samples are in good agreement with the photocatalytic activity under visible light illumination. The enhanced photocurrent density confirms the larger separation rate of the photoinduced electron-hole pairs in the 3-7 g-C_3N_4/$Bi_4O_5I_2$ heterojunction.

Generally, the PL intensity and the photoc3atalytic activity have strong correlation, because the PL spectra principally result from the recombination of photogenerated electron-hole pairs in a semiconductor. The low PL intensity suggests the decreased recombination rate of electrons and holes, which results in higher photocatalytic activity. The PL spectra of g-C$_3$N$_4$, Bi$_4$O$_5$I$_2$ and the as-prepared g-C$_3$N$_4$/Bi$_4$O$_5$I$_2$ composites are displayed in Fig. 8. The as-observed PL intensity follows the order: g-C$_3$N$_4$ > Bi$_4$O$_5$I$_2$ > 3-7 g-C$_3$N$_4$/Bi$_4$O$_5$I$_2$. The emission intensity of 3-7 g-C$_3$N$_4$/Bi$_4$O$_5$I$_2$ is much smaller than that of g-C$_3$N$_4$, indicating that the electron-hole recombination process is suppressed in the heterojunction. This is also ascribed to the photogenerated electron transfer between g-C$_3$N$_4$ and Bi$_4$O$_5$I$_2$.

To elucidate the band structure of g-C$_3$N$_4$/Bi$_4$O$_5$I$_2$ heterojunction, electrochemical flat potential measurements by Mott-Schottky methods were carried out, and the data were shown in Fig. 9. The flat potentials of g-C$_3$N$_4$ and Bi$_4$O$_5$I$_2$ are calculated to be -1.07 and -0.35 eV, respectively, versus the saturated calomel electrode (SCE), which are equivalent to -0.83 and -0.11 eV versus the normal hydrogen electrode (NHE).[37] It is known that the conduction band position of *n*-type semiconductors is 0.1-0.3 eV higher than the flat potentials, depending on the electron effective mass and carrier concentration.[38,39] Here, the voltage difference between the conduction band and the flat potential is set to be 0.3 eV, and therefore the bottom of the conduction band for g-C$_3$N$_4$ and Bi$_4$O$_5$I$_2$ are -1.13 and -0.41 eV. And the VB of g-C$_3$N$_4$ and Bi$_4$O$_5$I$_2$ are 1.57 eV and 1.62 eV, respectively.

4. Conclusions

The g-C$_3$N$_4$/Bi$_4$O$_5$I$_2$ 2D-2D layered heterojunction has been synthesized and investigated as a visible-light driven photocatalyst for RhB degradation and NO removal. It was observed that the photocatalytic activity of Bi$_4$O$_5$I$_2$ is greatly influenced by the content of g-C$_3$N$_4$. The 3-7 g-C$_3$N$_4$/Bi$_4$O$_5$I$_2$ composite is found to be a more efficient photocatalyst than pure Bi$_4$O$_5$I$_2$ and g-C$_3$N$_4$. During 40 min of visible light irradiation, 99% of RhB ($1*10^{-5}$ mol•L^{-1}) is degraded using 1 g/L of 3-7 g-C$_3$N$_4$/Bi$_4$O$_5$I, and 51% of NO (100 ppm) is removed after 30 min illumination over 0.3 g/L of 3-7 g-C$_3$N$_4$/Bi$_4$O$_5$I$_2$. The electron-hole separation and transfer in this n-n heterojunction is explained schematically through a probable mechanism. The enhanced photocatalytic activity of g-C$_3$N$_4$/Bi$_4$O$_5$I$_2$ heterojunctions should be mainly attributed to the high-efficient charge separation across their interface. These findings manifested that g-C$_3$N$_4$/Bi$_4$O$_5$I$_2$ can act as a promising photocatalyst for environmental purification.

Acknowledgement

Notes and references

Beijing Key Laboratory of Materials Utilization of Nonmetallic Minerals and Solid Wastes, National Laboratory of Mineral Materials, School of Materials Science and Technology, China University of Geosciences, Beijing 100083, PR China
Tel: 86-10-82323433; E-mail: zyh@cugb.edu.cn; hhw@cugb.edu.cn.

1   D. Aijun, S. Stefano, L. Zhen, D.W. Wang, Y. Jiao, T. Liao, Q. Sun, Y. Huang, Z.H. Zhu, R. Amal and S.C. Smith, *Am. Chem. Soc.* 2012, **134**, 4393.

2   Z. H. Ai, W. K. Ho, S. C. Lee and L. Z. Zhang, *Environ. Sci. Technol.* 2009, **43**, 4143.

3   K. Maeda, ACS Catal. 2013, **3**, 1486.

4   H. W. Huang, X. Han, X. W. Li, S. C. Wang, P. K. Chu and Y. H. Zhang, *ACS Appl. Mater. Inter.* 2015, **7**, 482.

5   J. Zhang, Y. H. Wang, J. Jin, J. Zhang, Z. Lin, F. Huang and J. G. Yu, *Appl. Mater. Inter.* 2013, **5**, 10317.

6   P. Sathishkumar, R. Sweena, J. J. Wu and S. Anandan, *Chem. Eng. J.* 2011, **171**, 136.

7   M. Yin, Z. Li, J. Kou and Z. Zou, *Environ. Sci. Technol.* 2009, **43**, 8361.

8   J. Jiang, L. Z. Zhang, H. Li, W. W. He and J. J. Yin, *Nanoscale.* 2013, **5**, 10573.

9   Y. N. Wang, K. J. Deng and L. Z. Zhang, *J. Phys. Chem. C.* 2011, **115**, 14300.

10   R. Li, X. Y. Gao, C. M. Fan, X. C. Zhang, Y. W. Wang and Y. F. Wang, *Appl. Surf. Sci.* 2015, **355**, 1075.

11   X. Xiao, C. L. Xing, G. P. He, X. X. Zuo, J. M. Nan and L. S. Wang, *Appl. Catal. B: Environ.* 2014, **148–149**, 154.

12   J. Yang, L. J. Xu, C. L. Liu, T. P. Xie, *Appl. Surf. Sci.* 2014, **319**, 265.

13   H. Liu, Y. Su, Z. Chen, Z. T. Jin and Y. Wang, *J. Mol. Catal. A-Chem.* 2014, **391**, 175.

14   X. C. Wang, K. Maeda, A. Thomas, K. Takanabe, G. Xin, J. M. Carlsson, K. Domen and M. Antonietti, *Nat. Mater.* 2009, **8**, 76.

15   Y. Wang, X. C. Wang and M. Antonietti, *Angew Chem. Int. Ed.* 2012, **51**, 68.

16   N. Tian, H. W. Huang, Y. He, Y. X. Guo, T. R. Zhang and Y. H. Zhang, *Dalton. T.* 2015, **44**, 4297.

17   N. Tian, H. W. Huang, Y. He, Y. X. Guo and Y. H. Zhang, *Colloid. Surface. A.* 2015, **467**, 188.

18   N. Tian, H. W. Huang, C. Y. Liu, F. Dong, T. R. Zhang, X. Du, S. X. Yu and Y. H. Zhang. *J. Mater. Chem. A*, 2015, **3**, 17120.

19   L. Q. Ye, J. Y. Liu, Z. Jiang, T. Y. Peng and L. Zan, Appl. *Catal., B: Environ.* 2013, **142-143**, 1.

20   X. J. Wang, Q. Wang, F. T. Li, W. Y. Yang, Y. Zhao, Y. J. Hao and S. J. Liu, *Chem. Eng. J.* 2013, **234**, 361.

21   J. Di, J. X. Xia, S. Yin, H. Xu, L. Xu, Y. G. Xu, M. Q. He and H. M. Li, *J. Mater. Chem. A.* 2014, **2**, 5340.

22   Z. Y. Wang, W. Guan, Y. J. Sun, F. Dong, Y. Zhou and W. K. Ho, *Nanoscale.* 2015, 7, 2471.

23   H. W. Huang, K. Liu, K. Chen, Y. L. Zhang, Y. H. Zhang and S. C. Wang, *J. Phys. Chem. C.* 2014, **118**, 14379.

24   N. Tian, H. W. Huang, Y. He, Y. X. Guo and Y. H. Zhang, *RSC Advances.* 2014, 4, 42716.

25   Q. C. Liu, D. K. Ma, Y. Y. Hu, Y. W. Zeng and S. M. Huang, *ACS Appl. Mater. Interfaces*, 2013, **5**, 11927.

26   G. Zhang, J. Zhang, M. Zhang and X. Wang, *J. Mater. Chem.* 2012, **22**, 8083.

27   J. Liu, T. Zhang, Z. Wang, G. Dawson and W. Chen, *J. Mater. Chem.* 2011, **21**, 14398.

28   Y. Wang, B. Li, C. Zhang, L. Cui, S. Kang, X. Li and L. Zhou, *Appl.Catal. B* 2013, **130-131**, 277.

29   Y. X. Yang, W. Guo, Y. N. Guo, Y. H. Zhao, X. Yuan and Y. H. Guo, *J. Hazard. Mater.* 2014, **271**, 150.

30   S. C. Yan, Z. S. Li and Z. G. Zou, *Langmuir.* 2010, **26**, 3894.

31   T. Montini, V. Gombac, A. Hameed, L. Felisari, G. Adami, and P. Fornasiero, *Chem. Phys. Lett.* 2010, **498**, 113.

32   O. Yayapao, T. Thongtem, A. Phuruangrat, and S. Thongtem, *J. Alloys Compd.* 2011, **509**, 2294.

33   J. F. Zhang, Y. F. Hu, X. L. Jiang, S. F. Chen, S. G. Meng and X. L. Fu, *J. Hazard. Mater.* 2014, **280**, 713.

34 H. W. Huang, X. W. Li, J. J. Wang, F. Dong, P. K. Chu, T. R. Zhang and Yihe Zhang. *ACS Catal.*, 2015, **5**, 4094.

35 H. W. Huang, Y. He, Z. S. Lin, L. Kang, and Y. H. Zhang, *J. Phys. Chem. C* 2013, **117**, 22986.

5 36 H. W. Huang, X. W. Li, X. Han, N. Tian, Y. H. Zhang and T. R. Zhang, *Phys. Chem. Chem. Phys.* 2015, **17**, 3673.

37 A. W. Bott, *Curr. Sep.* 1998, **17**, 87.

38 W. J. Luo, Z. S. Li, X. J. Jiang, T. Yu, L. F. Liu, X. Y. Chen, J. H. Ye and Z. G. Zou, *Phys. Chem. Chem. Phys.* 2008, **10**, 6717.

10 39 J. L. Wang, Y. Yu and L. Z. Zhang, *Appl. Catal. B* 2013, **136-137**, 112.

Journal Name

ARTICLE TYPE

5

10
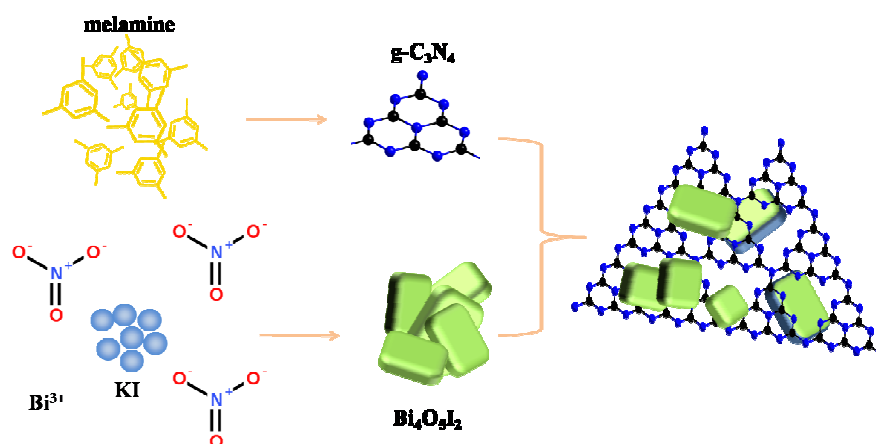
Scheme. 1 Schematic illustration for the formation process of g-C$_3$N$_4$/Bi$_4$O$_5$I$_2$.

15
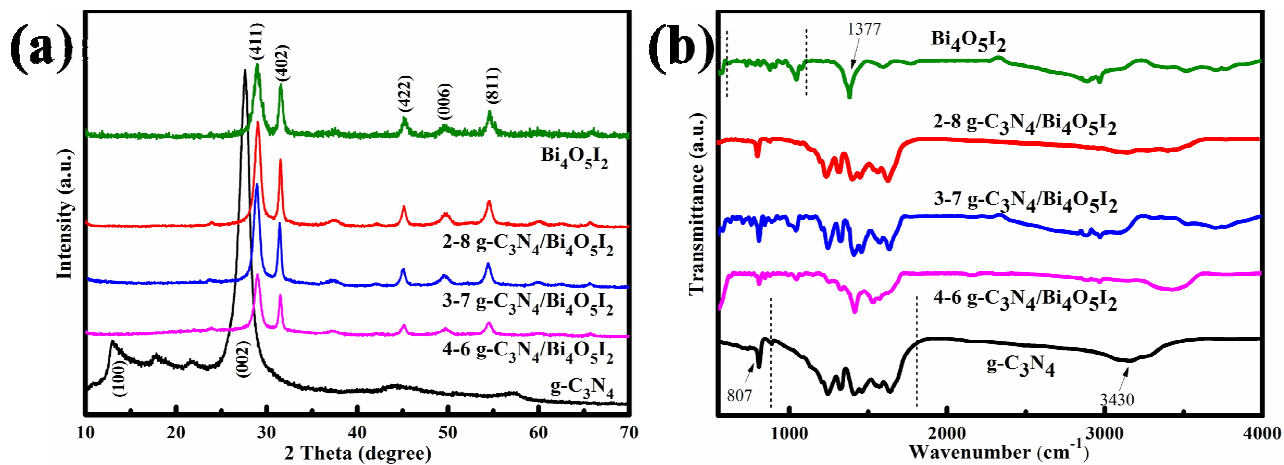
Fig. 1 (a) XRD patterns, and (b) FTIR spectra of g-C$_3$N$_4$, Bi$_4$O$_5$I$_2$ and g-C$_3$N$_4$/Bi$_4$O$_5$I$_2$ samples.
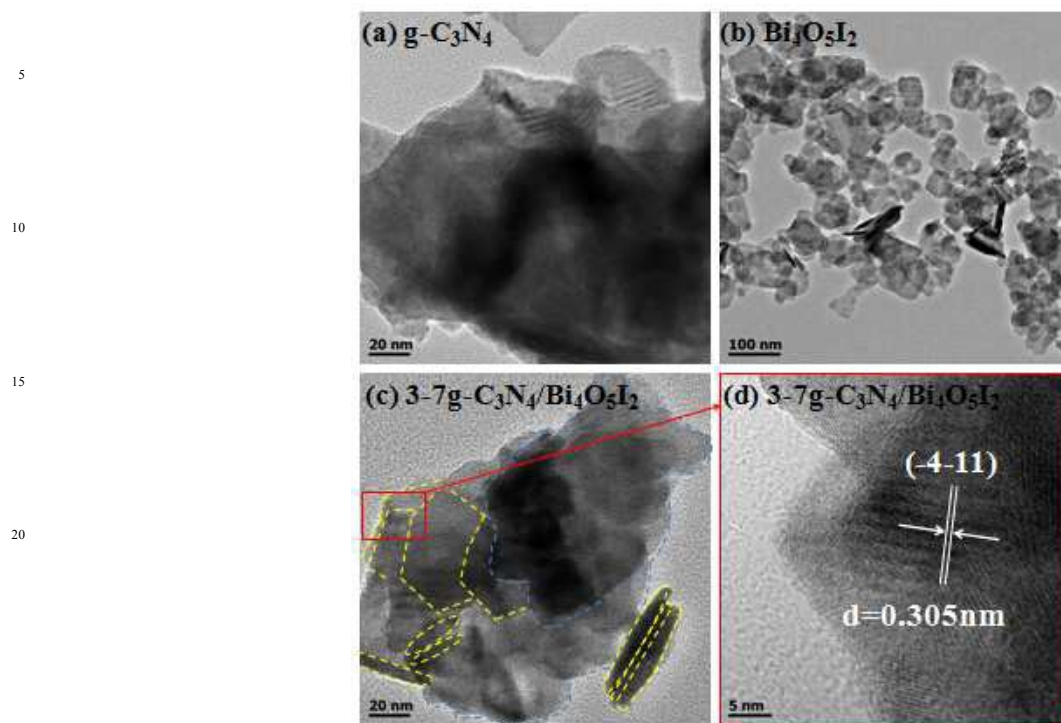
Fig. 2 TEM images of (a) g-C_3N_4, (b) $Bi_4O_5I_2$ and (c, d) 3-7 g-C_3N_4/$Bi_4O_5I_2$ samples.
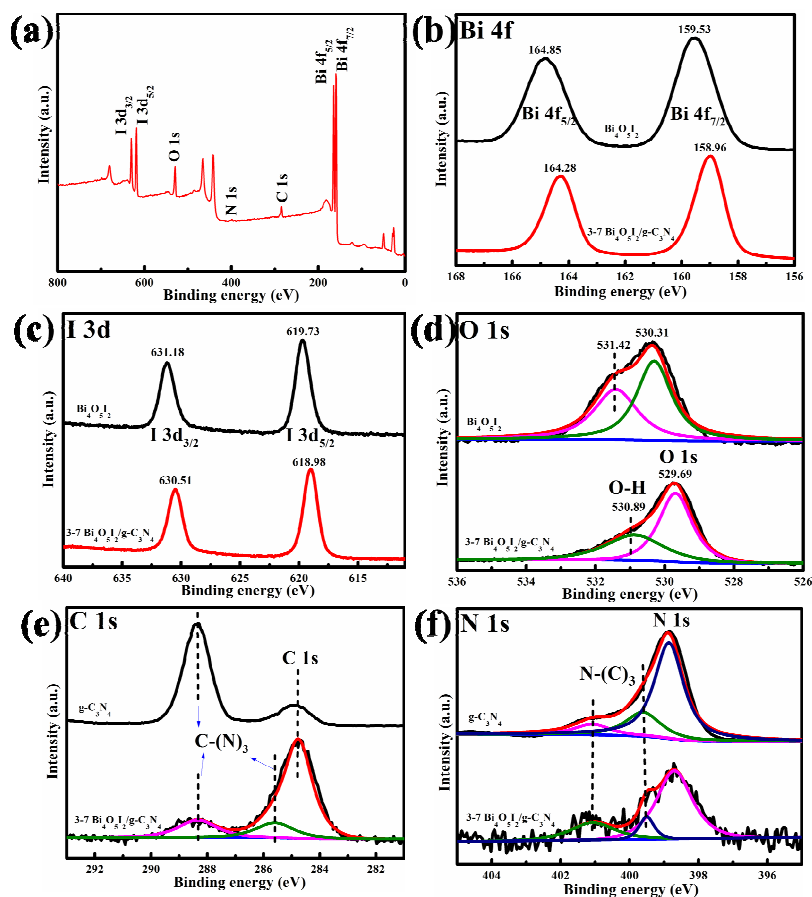
Fig. 3 (a) Typical XPS survey spectra of 3-7 g-C$_3$N$_4$/Bi$_4$O$_5$I$_2$. High resolution XPS spectra of (b) Bi 4f, (c) O 1s, (d) I 3d, (e) C 1s and (f) N 1s of 3-7 g-C$_3$N$_4$/Bi$_4$O$_5$I$_2$.
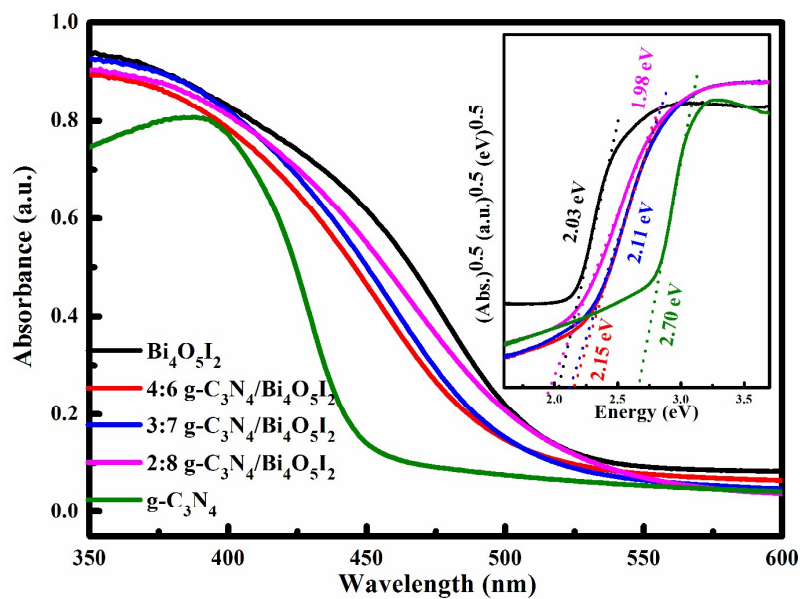
Fig. 4 UV-vis diffuse reflectance spectra of g-C_3N_4, $Bi_4O_5I_2$ and g-C_3N_4/$Bi_4O_5I_2$ samples. The inset is a plot of $(\alpha h \gamma)^{1/2}$ versus the energy (eV) for g-C_3N_4 and $Bi_4O_5I_2$.
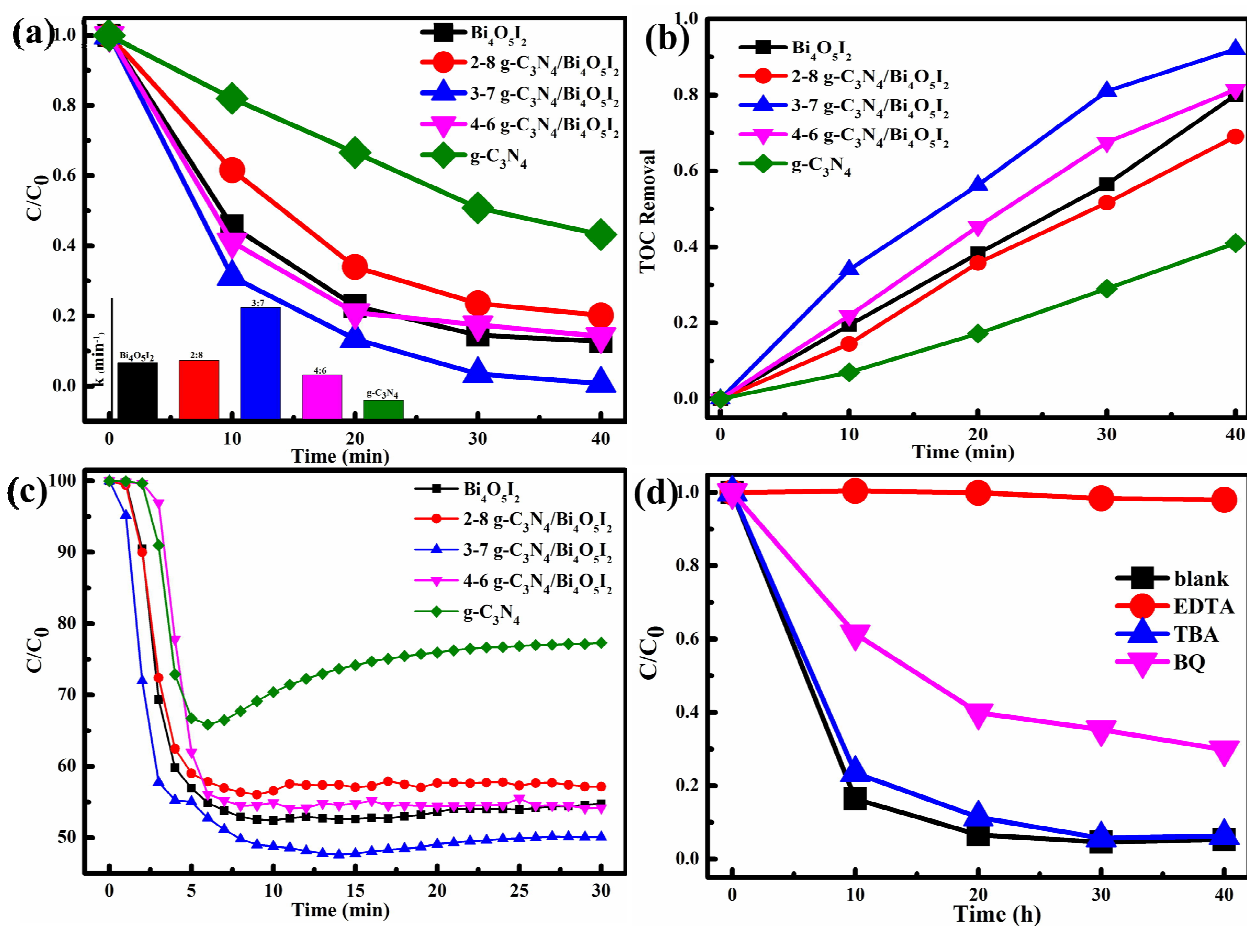
Fig. 5 (a) Photocatalytic degradation curves of RhB, the figure insert (a) is apparent rate constants for

5 the RhB degradation. (b) TOC removal efficiency and (c) Photocatalytic NO removal curves over g-C$_3$N$_4$, Bi$_4$O$_5$I$_2$ and g-C$_3$N$_4$/Bi$_4$O$_5$I$_2$ samples under visible light (λ > 420 nm) irradiation. (d) Photocatalytic degradation of RhB over 3-7 g-C$_3$N$_4$/Bi$_4$O$_5$I$_2$ photocatalysts alone and with the addition of EDTA, IPA, BQ, or nitrogen bubbling.

10
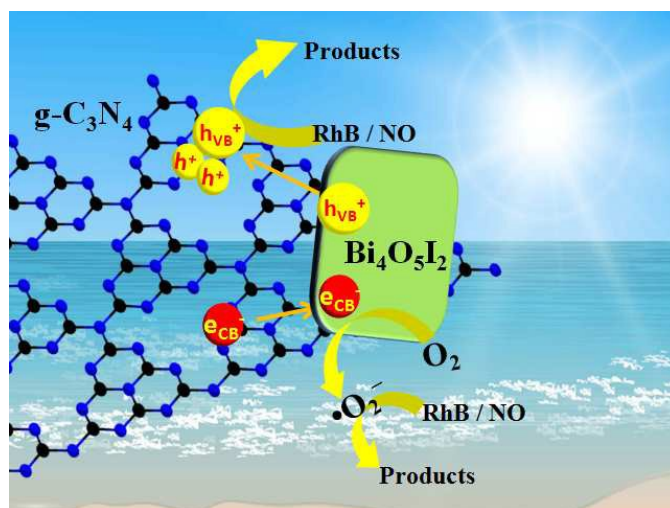
15

Fig. 6 Schematic diagram of electron-hole pairs separation and the possible reaction mechanism.
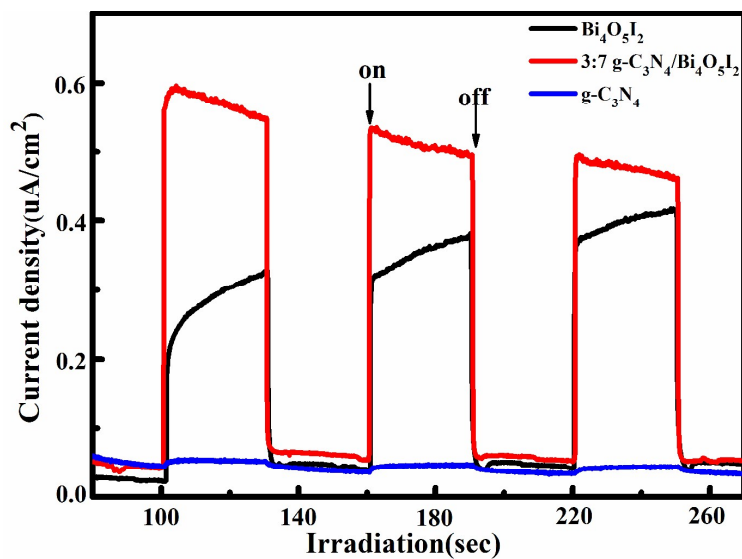
Fig. 7 Comparison of transient photocurrent response of g-C$_3$N$_4$ and Bi$_4$O$_5$I$_2$, and 3-7 g-C$_3$N$_4$/Bi$_4$O$_5$I$_2$.
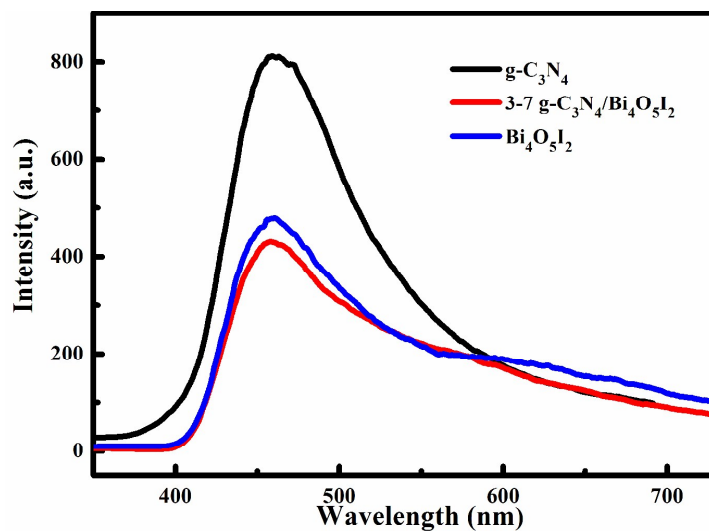
Fig. 8 Photoluminescence spectra of the g-C_3N_4, $Bi_4O_5I_2$ and 3-7 g-C_3N_4/$Bi_4O_5I_2$ samples.
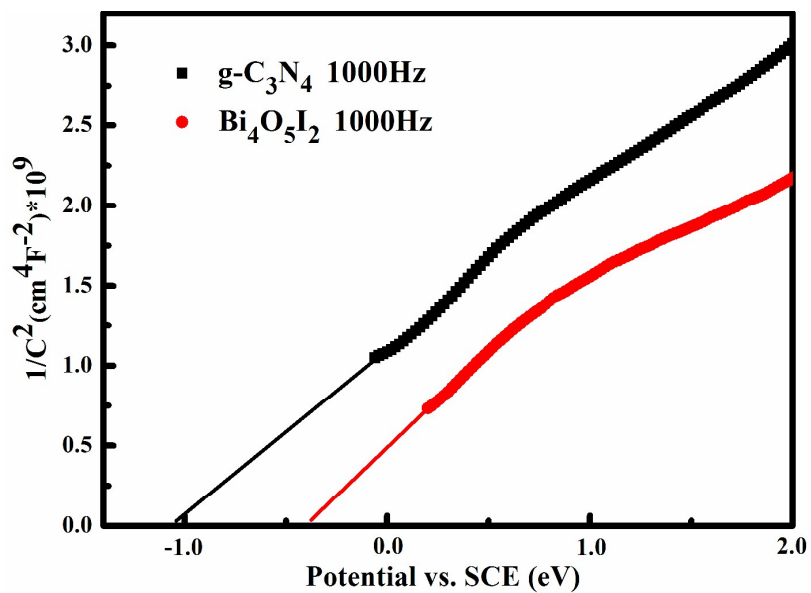
Fig.9 Mott-Schottky plots of pure g-C_3N_4 and $Bi_4O_5I_2$ film electrodes at a frequency of 1000 Hz in an aqueous solution of Na_2SO_4 (0.1 M).

Journal Name

ARTICLE TYPE

g-C₃N₄/Bi₄O₅I₂ 2D-2D heterojunctional nanosheets with enhanced visible-light photocatalytic activity

Na Tian, Yihe Zhang*, Chengyin Liu, Shixin Yu, Min Li, Hongwei Huang*

Beijing Key Laboratory of Materials Utilization of Nonmetallic Minerals and Solid Wastes, National Laboratory of Mineral Materials, School of Materials Science and Technology, China University of Geosciences, Beijing 100083, PR China

*Corresponding author. Tel.: +86-10-82323433.
E-mail address: zyh@cugb.edu.cn. (Y. H. Zhang); hhw@cugb.edu.cn (H. W. Huang).
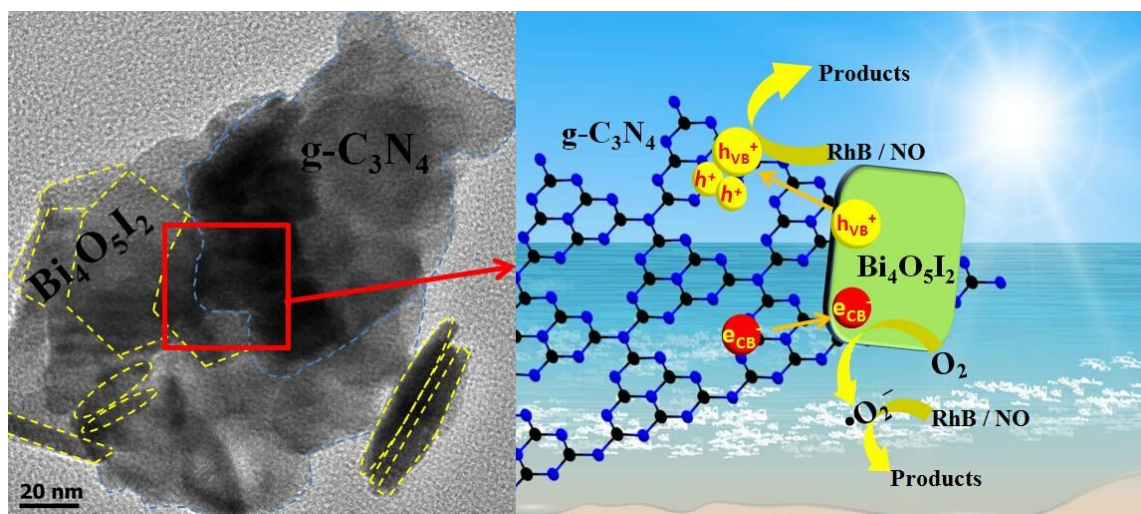
The 2D-2D heterojunctional g-C₃N₄/Bi₄O₅I₂ nanosheets were successfully constructed based on band gap engineering design. It exhibits high visible-light-driven photocatalytic activity for degradation of RhB and NO removal.